JOURNAL OF PROPULSION AND POWER
Vol. 25, No. 1, January–February 2009

Flame Stabilization in High-Pressure Liquid Oxygen/Methane Rocket Engine Combustion

Johannes Lux* and Oskar Haidn†
DLR, German Aerospace Center, 74239 Lampoldshausen, Germany

DOI: 10.2514/1.36852

Flame stabilization in the near-injector region of a subscale liquid propellant rocket combustion chamber has been investigated using optical diagnostics. Several different single shear coaxial injectors have been used to inject liquid oxygen (LOX) and methane at relevant operating conditions. Three main operating points cover the range of sub-, near-, and supercritical conditions with respect to the thermodynamic critical point of oxygen. Whereas liquid oxygen has been injected at typical temperatures of about 120 K, gaseous methane was injected at near-ambient temperatures of about 270 K. Similar to previous investigations performed with LOX/H_2 combustion, spontaneous OH chemiluminescence has been detected to characterize the flame anchoring zone near the LOX post tip. Theoretical considerations have indicated that the binary mixture of oxygen and methane shows an entirely different behavior compared with the oxygen/hydrogen system. This is believed to have an influence on the spray evolution and mixing characteristics at supercritical conditions. The experimental investigation includes both the ignition transient as well as the steady-state operating points. It has been detected that the LOX/CH_4 flame shows very similar characteristics in comparison with a LOX/H_2 flame at similar operating conditions. Critical flame stabilization at the startup transient has been found during all hot runs. At steady-state conditions, the influence of the injection parameters on the flame shape is comparable to previous LOX/hydrogen investigations.

Nomenclature

A	=	injection area, m^2
c_p	=	isobaric heat capacity, $J/(kg \cdot K)$
d_i	=	LOX jet diameter, mm
$\boldsymbol{e}_x$, $\boldsymbol{e}_y$	=	unit vectors in the x and y directions
G	=	magnitude of the gradient $\nabla \bar{I}_{OH}$
I	=	emission intensity
J	=	momentum flux ratio
k	=	binary interaction coefficient
$\dot{m}$	=	propellant mass flow, kg/s
P	=	pressure, bar
R	=	universal gas constant, $(Pa \cdot m^3)/(K \cdot mol)$
ROF	=	propellant mixture ratio, $\dot{m}_{O2}/\dot{m}_{CH_4}$
ROF_{global}	=	global propellant mixture ratio (including window cooling mass flow)
T	=	temperature, K
t	=	injector wall thickness, mm
u	=	injection velocity, m/s
v	=	molar volume, m^3/mol
x	=	mole fraction of the gas phase
y	=	mole fraction of the liquid phase
λ	=	thermal conductivity, $W/(m \cdot K)$
ρ	=	density, kg/m^3
σ	=	surface tension, N/m

Subscripts

c	=	critical value
cc	=	combustion chamber
g	=	gaseous
i, o	=	inner, outer
i, j	=	species
l	=	liquid
mix	=	mixture value
r	=	reduced value

Received 27 January 2008; revision received 3 May 2008; accepted for publication 1 June 2008.

*Ph.D. Student, Research Engineer, Institute of Space Propulsion; johannes.lux@dlr.de.

†Head of Technology, Institute of Space Propulsion. Associate Fellow AIAA.

I. Introduction

TODAY'S high-performance liquid propellant rocket engines, such as the space shuttle main engine (SSME) and the main engine of the European launcher Ariane 5 Vulcain II, are operated with the cryogenic propellant combination LOX/H_2 due to its high specific impulse. To reduce operational costs as well as overall propellant tank sizes, the development of future launch vehicles considers hydrocarbon propellants especially for applications in booster or core stage engines. In this context, the most promising propellant combination is LOX/methane. Compared with LOX/kerosene, it shows a better overall performance from a system point of view [1]. Methane can be extracted from natural gas and provides a density 6 times higher than hydrogen when stored in a liquid state at typical tank pressures.

Although the propellant combination LOX/H_2 has been investigated extensively by different research groups during the last decades [2–5], no or only few experimental data are available for LOX/CH_4 combustion at relevant high-pressure conditions [6–8]. Numerical simulations concerning the flame anchoring mechanisms in LOX/CH_4 coaxial injection have been performed by Zong and Yang [9] and Zong et al. [10]. The design and optimization of modern liquid propellant rocket engines using hydrocarbon fuels require a detailed understanding of the dominating physical phenomena at high-pressure coaxial injection and combustion. Fundamental experimental data are necessary for the validation of numerical tools. Observations of both high-pressure cold flow experiments and LOX/H_2 combustion have shown significant disparities in the atomization processes at sub-, near-, and supercritical injection conditions [11,12]. First experimental investigations with an application of optical diagnostics of LOX/CH_4 combustion at elevated pressures have been performed using an additional methane fluid system implemented at the European Research and Test Facility P8 [13]. An extensive test series has been realized, which has led to a well-defined and representative database for LOX/Methane combustion at high-pressure conditions combined with typical main chamber mixture ratios.

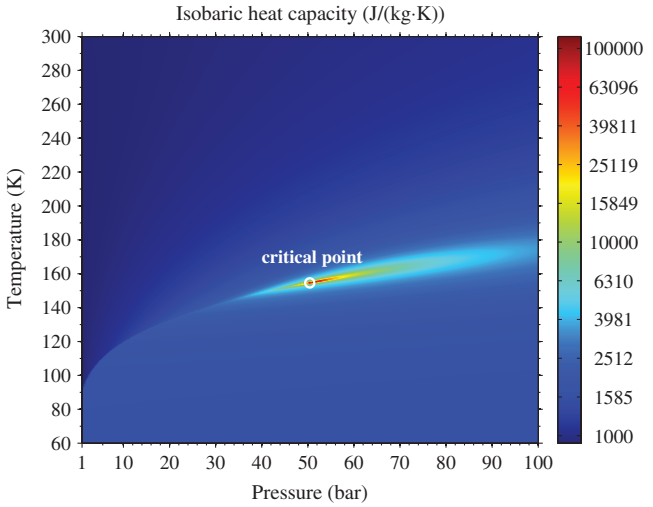

Fig. 1 Isobaric heat capacity of oxygen [14,31].

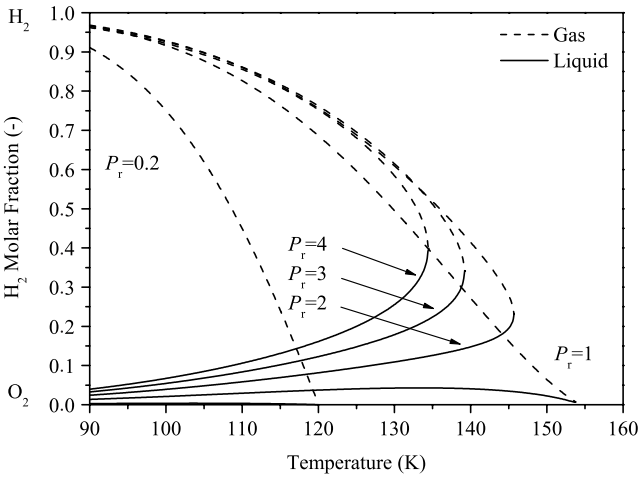

Fig. 2 Phase equilibrium of the H_2/O_2 system.

II. Thermodynamic Properties

Modern liquid propellant rocket engines usually operate at pressures near or above the critical pressure of oxygen ($P_{c,O_2} = 50.43$ bar). A potential LOX/CH_4 booster engine would probably be operated at pressures above 130 bar, whereas a cryogenic upper stage engine could also be operated at near critical pressures far below 100 bar. For example, the cryogenic LOX/H_2 upper stage engine Vinci, currently under development, is operated at about 60 bar. The reduced pressure P_r is defined with respect to the thermodynamic critical point of oxygen:

$$P_r = P_{cc}/P_{c,O_2} \tag{1}$$

Near the critical point, thermodynamic fluid properties like the density ρ and the thermal conductivity λ show extreme gradients. The surface tension σ tends toward zero and vanishes above the critical point. At the critical point, the isobaric heat capacity c_p tends toward infinity, as shown in Fig. 1. For the calculation of all pure fluid properties and mass flows, an equation of state in the form of the Helmholtz free energy has been used for oxygen and methane [14,15]. The critical fluid properties of hydrogen, oxygen, and methane are shown in Table 1. It becomes apparent that the critical points of oxygen and methane are closer to each other than is the case with oxygen and hydrogen.

Above the critical point, fluids behave like dense gases and the atomization and mixing in coaxial injection is driven by turbulence and diffusion processes. At subcritical pressures, the atomization process is more influenced by surface tension. As shown in previous publications, a phase equilibrium between hydrogen and oxygen can exist at pressures above the critical pressure of both pure fluids [17,18]. For the calculation of thermodynamic properties of a binary mixture under high-pressure conditions, a suitable equation of state is required. The classical criterion for a vapor–liquid equilibrium is equal fugacity in both phases for each single component at a uniform temperature and pressure. The conventional Redlich–Kwong equation of state has been used to calculate the equilibrium. It is shown in Eq. (2) for the calculation of pure fluid properties. The fluid specific parameters a and b depend on both the critical temperature T_c and the critical pressure P_c, as shown in Eqs. (3) and (4).

Table 1 Thermodynamic fluid properties at the critical point [14–16]

	Methane	Oxygen	Hydrogen
T_c, K	190.564	154.581	32.9380
P_c, bar	45.992	50.430	12.8377
ρ_c, kg/m^3	162.660	436.144	31.3600

$$P = \frac{RT}{(v-b)} - \frac{a}{\sqrt{T}\cdot v\cdot(v+b)} \tag{2}$$

$$a = \frac{0.42748\cdot R^2\cdot T_c^{2.5}}{P_c} \tag{3}$$

$$b = \frac{0.08664\cdot R\cdot T_c}{P_c} \tag{4}$$

For a mixture consisting of n components, the parameters a_{mix} and b_{mix} are calculated using the pure fluid parameters in combination with an additional mixing rule:

$$a_{\text{mix}} = \sum_{i=1}^{n}\sum_{j=1}^{n} y_i x_j \sqrt{a_i a_j}(1-k_{ij}) \tag{5}$$

$$b_{\text{mix}} = \sum_{i=1}^{n} y_i b_i \tag{6}$$

The binary interaction coefficient k_{ij} can be determined from experimental data for a binary mixture. Because no experimental data are available for the corresponding systems, it has been set to zero as suggested by other authors [19]. The calculated phase equilibrium of the H_2/O_2 system at elevated pressures up to 200 bar is shown in Fig. 2.

The same set of equations has been used to calculate the phase equilibrium of the binary system CH_4/O_2 [20]. It is shown in Fig. 3 for five different pressure levels. The system shows a different behavior compared with the H_2/O_2 system. No phase equilibrium can be found above the reduced pressure of $P_r = 0.935$. In contrast to the H_2/O_2 system, the temperature ranges of phase equilibria are much smaller. According to Nicoli et al. [21], the CH_4/O_2 system is a type I.a system with a bounded liquid–vapor equilibrium. By contrast, the H_2/O_2 system can be assigned to the type I.b system, which typically features an unbounded liquid–vapor equilibrium. It follows from this that no surface tension exists for the binary mixture CH_4/O_2 above $P_r = 0.935$ (47.15 bar).

The model of a binary mixture is only a first approximation. Products from the H_2/O_2 and CH_4/O_2 reactions, like water vapor, are neglected and should be considered in a more detailed model. However, it could be assumed that the transcritical and supercritical behavior of a nonreacting LOX/CH_4 coaxially injected spray is slightly different from that of an H_2/O_2 spray.

To get a better understanding of the flame stabilization processes in high-pressure conditions, the coaxial injection of LOX/CH_4 has been investigated using an optically accessible model combustor.

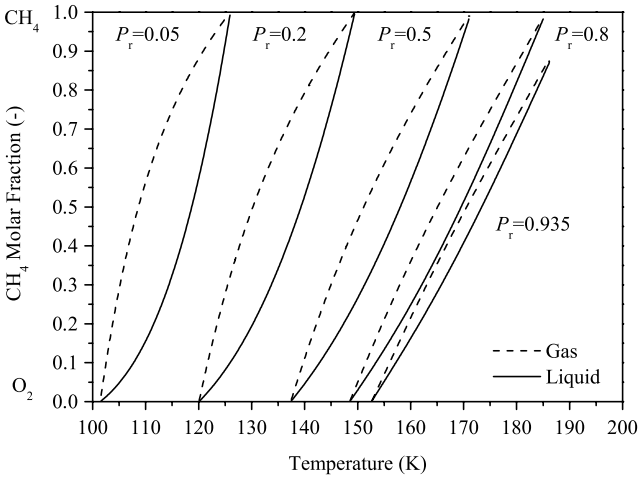

Fig. 3 Phase equilibrium of the CH_4/O_2 system.

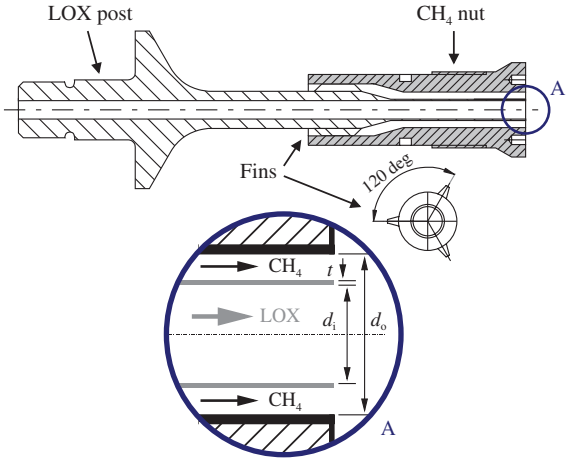

Fig. 5 Single shear coaxial injector element.

III. Thrust Chamber and Injector Element

The DLR subscale combustion chamber C used for the investigations can be operated at steady-state conditions and pressures of up to 100 bar. It is shown in Fig. 4. The maximum time of a hot run is only limited by the capabilities of the test bench. Chamber C is water cooled and features a total length of 430 mm with an inner diameter of 50 mm. The throat diameter is 17.3 mm. Four quartz glass windows are available for optical access to the near-injector region. A hydrogen film cooling mass flow at ambient temperatures protects the windows and the chamber walls from the hot gases during operation. The cooling mass flow has been regulated at 160–230 g/s to provide a constant injection velocity. It is believed that the hydrogen film does not affect the near-injector LOX/methane flame stabilization. However, the global combustion process is influenced by the film cooling mass flow; thus, combustion efficiency has not been calculated within this investigation.

High-precision static and dynamic pressure transducers have been used at a data acquisition rate of 100 Hz and 100 kHz, respectively. The volume flows of liquid oxygen, gaseous hydrogen, and gaseous methane have been determined using flow turbines. The resulting mass flows have been determined with a density calculation using the aforementioned equations of state. The total resulting mass flow measurement error can be assumed to be less than 2%. High-precision temperature measurements are provided by several thermocouples in the domes, in the chamber, and in the cooling water supply system. The accuracy of the temperature measurement is ±1.25 K [12]. Because it is not possible to measure the fluid temperatures directly before entering the combustion chamber, injection conditions are calculated based on the combustion chamber pressure and the fluid dome temperatures. With this approach, the heat transfer between the liquid oxygen and the methane within the injection element is neglected.

The injector element used in the present study is a single shear coaxial element without recess and tapering, as shown in Fig. 5. The LOX post has an inner diameter, d_i, of 5.6 mm and a standard wall thickness, t, of 0.3 mm ($0.054d_i$). Singla et al. [22] recently proposed thicker lip sizes, especially for the injection of LOX/methane compared with LOX/H_2. In this context, the influence of the injector wall thickness on the flame stabilization in LOX/CH_4 combustion at elevated pressures should be investigated systematically. The coaxial CH_4 slot of the injector element is defined by an interchangeable nut with an outer diameter, d_o, of 7–8 mm ($1.25–1.43d_i$). A total LOX tube length of about $20d_i$ ensures a well-established velocity profile. The injector element features typical dimensions of coaxial injector elements used in modern liquid propellant rocket engines, such as the SSME and the main engine of the European launcher Ariane 5 Vulcain II.

IV. Operating Conditions

The combustion chamber was operated at three steady-state operating points representing sub-, near-, and supercritical conditions. In conformance with previous investigations using the propellant combination LOX/H_2, phase 1 represents supercritical conditions at about 60 bar ($P_r > 1$), and phase 2 ($P_r \approx 1$) and phase 3 ($P_r < 1$) refer to near- and subcritical conditions, respectively. Because of the blowdown mode of the test facility, the operating

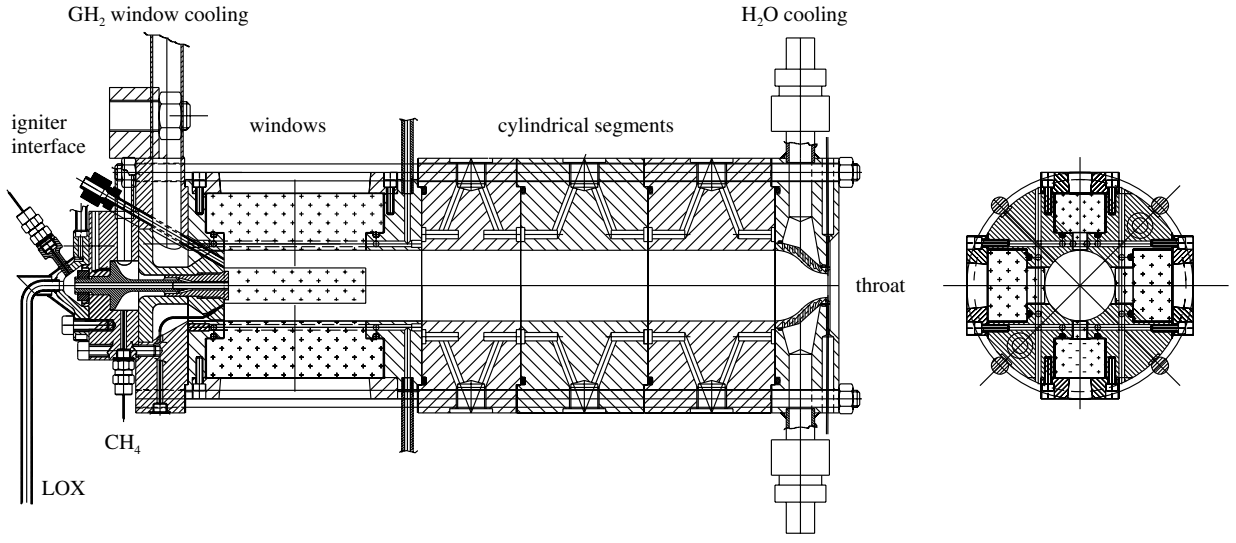

Fig. 4 Combustion chamber C with window segment and implemented single shear coaxial injector element.

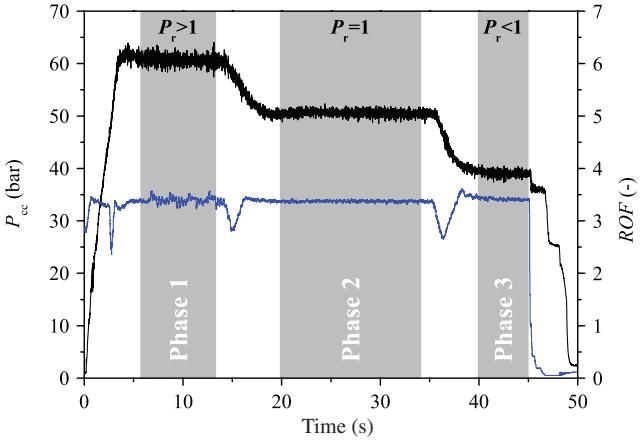

Fig. 6 Pressure trace of a typical hot run.

sequence starts with phase 1 as the first steady state. It is assumed that the order of the three steady states does not influence the results at all. Figure 6 shows the pressure and mixture ratio traces of a typical three-step hot run.

The mixture ratio ROF was held constant at 3.4 throughout all tests. Liquid oxygen was injected at 120 K whereas gaseous methane was maintained at about 270 K. The injection velocity ratio (VR) and the momentum flux ratio J are commonly believed to have an influence on the atomization process in coaxial injection:

$$\mathrm{VR} = u_g/u_l \tag{7}$$

$$J = \frac{(\rho \cdot u^2)_g}{(\rho \cdot u^2)_l} \tag{8}$$

Because surface tension vanishes above the critical point, the Weber number was not taken into account for the characterization of the atomization within the present investigation. As per Eqs. (7) and (8), the velocity ratio and momentum flux ratio are strongly related to each other within the corresponding operating conditions. Both numbers are connected with the injection area ratio $\mathrm{AR} = A_g/A_l$ and the mixture ratio:

$$\mathrm{VR}/J = \mathrm{AR} \cdot ROF \tag{9}$$

Within this investigation, most results are presented depending on the momentum flux ratio. Values have been varied between VR = 7–28 and $J = 3$–25. Typical operating conditions are given in Table 2. Methane injection velocities $v_{\mathrm{CH_4}}$ as well as the resulting VRs and J depend on the injection diameter d_o. Therefore, operating conditions for the specific points A–D (shown in Fig. 15) are given in Table 2.

V. Optical Diagnostics

Spontaneous OH and CH chemiluminescence have been detected using an identical pair of intensified high-speed charge-coupled device (CCD) Photron FASTCAM Ultima APX I^2 cameras. Both systems are equipped with a 10 bit complimentary metal-oxide semiconductor sensor, an appropriate UV image intensifier, and a fixed focal length 105 mm 1:4.5 Nikon Nikkor UV lens. A typical optical setup is shown in Fig. 7. Because both systems are arranged in a fully symmetrical setup, all emission images are of the same dimensions and thus very comparable. Narrowband filters have been used to detect OH emission at 308 ± 5 nm and CH emission at 430 ± 3 nm. Because of the fact that the available optical resolution decreases with increasing frame rate, a good compromise is required to meet all objectives of the investigation. Therefore, the optical resolution was set to 1024×256 pixels at a frame rate of 8 kHz. That allowed a relatively good optical resolution of the full window section including the anchoring zone at the injector. To get nearly instantaneous images, a short exposure time is desirable. With the image intensifiers used within this investigation, an exposure time as low as 10 μs could have been realized at a good signal-to-noise ratio covering the full dynamic range of the system. It has been shown that there are no or only tiny differences visible between OH and CH emission images. Taking into account the slightly different gain characteristics of the two image intensifiers as well as the signal-to noise-ratio, tracing back these differences to physical phenomena does not seem to be meaningful. Similar observations have been reported by Richecoeur et al. [23]. To omit additional mirrors and lenses and to get the best possible emission images, no shadowgraphy setup has been used. Some basic shadowgraph images covering similar operating conditions have been presented by Lux et al. [13].

Flame emission spectra have been recorded during several hot runs covering all operating conditions. A 46 cm HR460 (1200 grooves/mm) Jobin Yvon spectrograph was used with an acquisition system consisting of an Andor intensified 256×1024 pixels CCD detector and the Andor data acquisition software. The spectral range was set for 250–700 nm with a resolution of 0.55 nm. The detector was focused on an area of 20 mm in diameter at a position 70 mm ($12.5 d_i$) downstream the faceplate. The acquisition rate was 9 Hz.

Table 2 Typical operating conditions

	Phase 1	Phase 2	Phase 3
P_r	1.18	1.00	0.80
T_{LOX}, K	120.2	121.1	123.9
$T_{\mathrm{CH_4}}$, K	282.6	279.9	277.2
ROF	3.40	3.42	3.36
$\dot{m}_{\mathrm{LOX}}$, g/s	302.4	253.0	201.9
$\dot{m}_{\mathrm{CH_4}}$, g/s	89.03	74.01	60.02
u_{LOX}, m/s	12.32	10.40	8.50
Operating point A			
$u_{\mathrm{CH_4}}$, m/s	90.92	89.75	92.06
VR	7.44	8.63	10.83
J	2.69	3.10	3.95
Operating point B			
$u_{\mathrm{CH_4}}$, m/s	118.3	117.0	119.6
VR	9.82	11.47	14.39
J	4.70	5.45	6.94
Operating point C			
$u_{\mathrm{CH_4}}$, m/s	150.2	148.4	151.2
VR	12.20	14.26	17.78
J	6.90	8.02	10.16
Operating point D			
$u_{\mathrm{CH_4}}$, m/s	230.2	227.3	230.7
VR	19.33	22.67	28.38
J	16.92	19.68	25.04

VI. Experimental Results

Different test campaigns have been performed at the European High Pressure Research and Technology Test Facility P8. Both transient and steady-state operating conditions have been investigated in detail to get a representative database at relevant conditions.

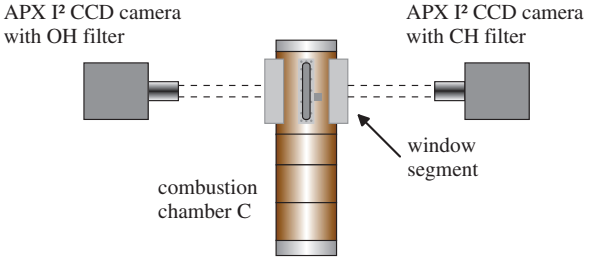

Fig. 7 Optical setup for emission imaging.

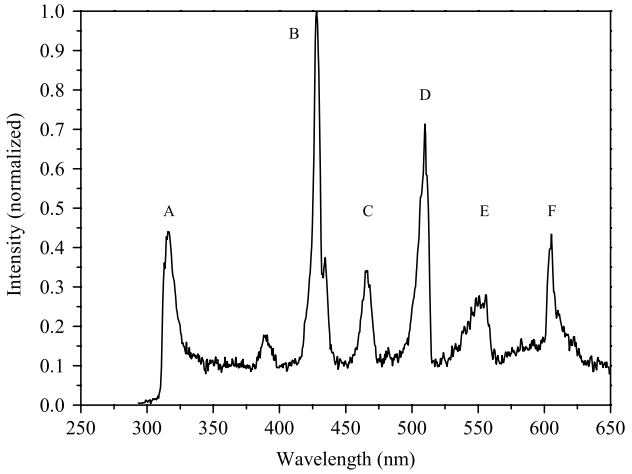

Fig. 8 Typical CH_4/O_2 flame emission spectrum from Bunsen burner at ambient pressure.

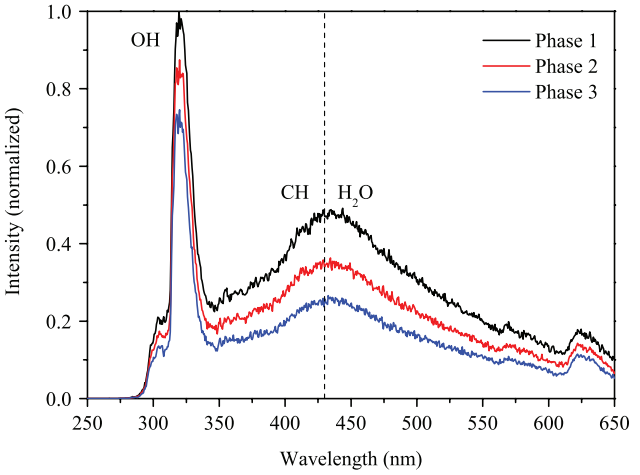

Fig. 9 Typical LOX/CH_4 flame emission spectrum (hydrogen window cooling mass flow).

A. Flame Emission Spectra

First, the CH_4/O_2 flame emission of a nitrogen-shielded Bunsen burner at ambient pressure was detected. For a mixture ratio of $ROF = 3.2$, the normalized spectrum is shown in Fig. 8. Table 3 gives details about peaks A–F. In addition to the OH and CH peaks, several C_2 emission peaks are well pronounced (C–F). With this configuration, the CH emission intensity is more than double the OH emission.

The same configuration was then used to detect the flame emission in LOX/CH_4 combustion during several steady-state operating points at the three main pressure levels. A representative spectrum for a mixture ratio of $ROF = 3.4$ is shown in Fig. 9. It is evident that the relative emission intensity strongly relates to the combustion chamber pressure. The OH emission peaks at 300–320 nm, whereas the CH emission is not as strongly emphasized. In contrast to the emission spectra of CH_4/O_2 flames at ambient pressure, as shown in Fig. 8, the strong and separated CH peak is not visible. Several peaks between 400 and 500 nm could be assigned to H_2O emission, similar to those discovered by Mayer et al. [24] for high-pressure LOX/hydrogen flames. Nevertheless, because the second emission peak is located at about 430 nm, high-speed CH emission detection was done as described earlier. It should be noted that a very similar spectrum was recorded when the chamber was operated with a gaseous methane window cooling mass flow. In that case, the maximum around 430 nm was increased by about 50% (relative to the OH emission peak) compared with the one detected with hydrogen window cooling. The ratio between the CH emission peak and the OH emission peak is given in Table 4 for both methane and hydrogen window cooling. It turned out that the total OH emission intensity is about 10% stronger with hydrogen window cooling.

Table 3 Detected CH_4/O_2 flame emission peaks

Peak	Species	Wavelength, nm	Transition
A	OH	306.4	$A^2\Sigma+, 0 - X^2\Pi, 0$
B	CH	431.2	$A^2\Delta, 0 - X^2\mathrm{N}, 0$
C	C_2	466.9	$A^3\Pi_g, 6 - X^3\Pi_u, 5$
D	C_2	509.8	$A^3\Pi_g, 2 - X^3\Pi_u, 2$
E	C_2	447–563.6	$A^3\Pi_g, 4 - X^3\Pi_u, 5$
F	C_2	605.9	$A^3\Pi_g, 2 - X^3\Pi_u, 4$

Table 4 Flame emission ratio CH/OH

	Phase 1	Phase 2	Phase 3
CH_4 *window cooling*			
P_r	1.11	0.94	0.75
ROF	3.10	3.10	3.10
ROF_{global}	0.77	0.64	0.45
Ratio CH/OH	0.94	0.91	0.71
H_2 *window cooling*			
P_r	1.18	0.99	0.79
ROF	3.39	3.42	3.36
ROF_{global}	0.93	0.93	0.91
Ratio CH/OH	0.49	0.42	0.36

B. Ignition Transient

Combustion chamber C is equipped with a gaseous oxygen/gaseous hydrogen torch igniter that is fired for less than a second during startup. It is equipped with a supply system independent of the main injector supply system. Because the startup transient is one of, if not the most, dangerous event in the life of a rocket engine, early and safe flame anchoring and stabilization is required. A stable flame anchoring is necessary to prevent blowoff or combustion instability triggering mechanisms [22]. A typical pressure trace during startup is shown in Fig. 10. P_{LOX} and $P_{\mathrm{CH_4}}$ represent the LOX and the methane dome pressures, respectively. $P_{\mathrm{vap,O_2}}$ represents the oxygen vapor pressure based on the oxygen temperature inside the dome. Ignition takes place at about 0.5 s and results in an abrupt pressure rise of about 5 bar. The chamber pressure then increases continuously up to the first steady-state level.

Instantaneous OH emission images taken during the startup transient are shown in Figs. 11a–11c. The injector is located on the left side with the methane injection nut extending into the image by about 3 mm. Because of the very different total intensity, every image has been colored using a scaled version of the color map to visualize the major characteristics of the flame. Hence, the total intensities of

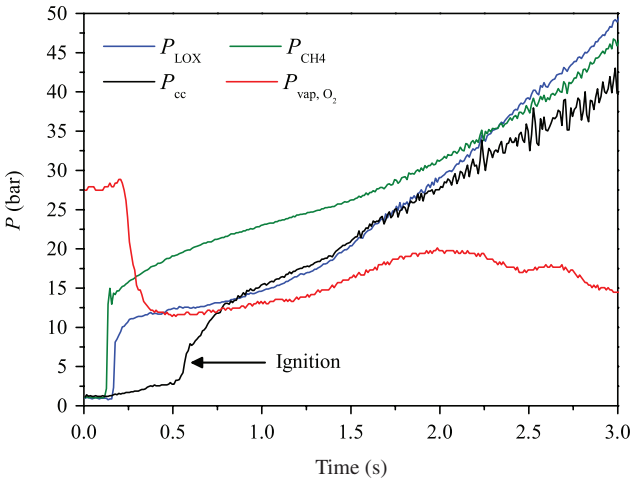

Fig. 10 Pressure trace during the ignition transient.

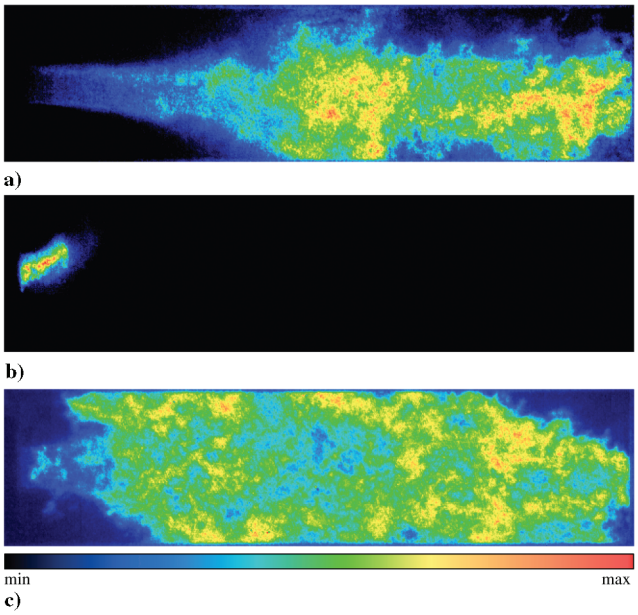

Fig. 11 Normalized OH emission during the ignition transient: a) $t_1 = 0.60$ s, b) $t_2 = 1.10$ s, and c) $t_3 = 3.06$ s.

the images shown in Figs. 11a–11c should not be compared with each other. At $t_1 = 0.60$ s, the flame already covers the full window section. The spreading is small and the total emission intensity is very low. Because of this low emission intensity, it is not possible to detect a flame anchoring at the LOX post tip. A stabilization at a point shortly behind the LOX post could also be possible. At $t_2 = 1.10$ s, the flame seems to collapse and is almost blown off. Only a very small flame is visible right behind the LOX post of the injector. The last image, at $t_3 = 3.06$ s, shows a normal, stabilized flame with typical spreading and high emission intensity. Figure 12a shows the evolution of the total emission intensity whereas Fig. 12b shows the axial flame dimension. It has been detected using a threshold technique, as illustrated in Fig. 13. As shown in Fig. 10, the oxygen vapor pressure is above the chamber pressure during the first 0.78 s of the ignition transient. Therefore, it can be assumed that the emission image in Fig. 11a shows a gaseous oxygen/gaseous methane flame. Sonic injection of both oxygen and methane and, thus, the resultant very low velocity ratio (VR < 3) lead to a stretched flame, as shown in Fig. 12b. As soon as the chamber pressure exceeds the vapor pressure of oxygen, liquid oxygen enters the combustion chamber at a much lower velocity based on the increased density. That leads to an abrupt shortage of the flame and a stabilization in the wake of the LOX post. Figure 13a shows the burning liquid oxygen jet. The image was taken shortly after the one shown in Fig. 11b. From that point, the flame grows again at a typical velocity ratio of VR > 20.

This ignition characteristic has been found during all test campaigns with both hydrogen and methane window cooling mass flow. It seems to be independent of the igniter sequence. First, ignition takes place as soon as the igniter flame enters the combustion chamber. High-speed emission images indicate a very small flame at the main injector that keeps the combustion process alive. The characteristic described earlier (including the pressure peak) is based on both the injection conditions and the thermodynamic state of the propellants. Especially the gaseous or two-phase flow of the oxygen as well as the liquefaction of gaseous oxygen inside the dome seems to be very dangerous with regard to a safe flame stabilization during the startup. In the case of a real engine, which is typically equipped with up to 600 injector elements, the risk of a flame blowoff during the startup transient could be reduced by implementing different injector geometries. In this context, it should be noted that recently investigated porous injectors as presented in Lux et al. [25] have shown a similar ignition characteristic. However, due to the very small LOX tube diameters of 1.8 mm in combination with much lower fuel injection velocities, the flame stabilization at t_2 (see Fig. 11b) seems to be less critical compared with the one presented

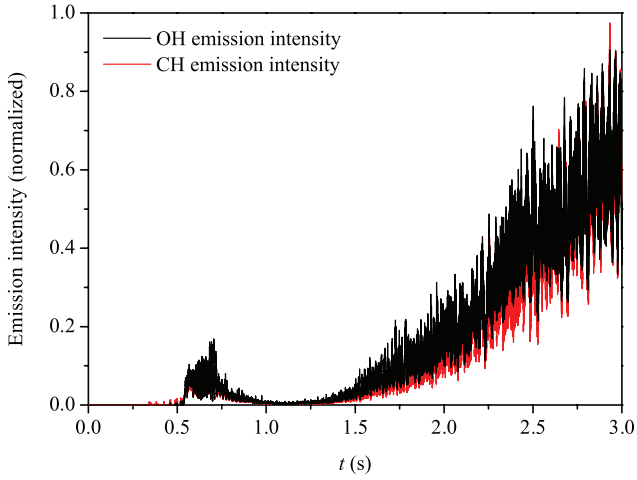

a) Normalized OH and CH emission intensity

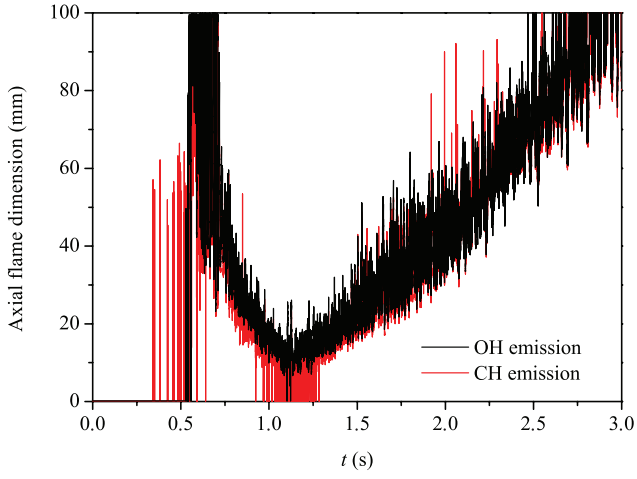

b) Axial flame dimension

Fig. 12 Evolution of the flame emission during startup.

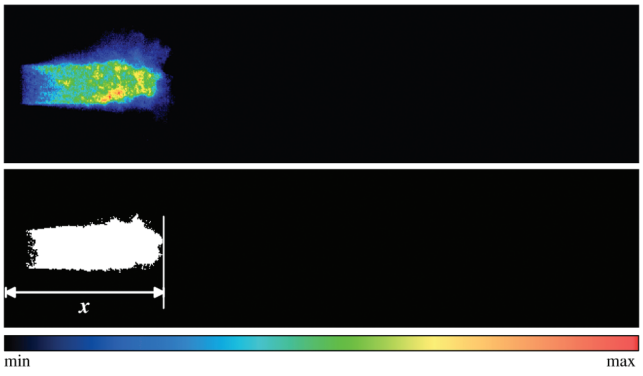

Fig. 13 Detection of the axial flame dimension, $t = 1.11$ s.

here. The LOX jet disintegration with the injection concept using a porous faceplate is not based on strong shear forces between the propellant components. With an increased fuel injection area, the VR is about unity and, thus, much lower compared with typical coaxial injection. Furthermore, the total number of injector elements increases by a factor of about 4–5 with the porous injection concept, which reduces the risk of a flame blowoff as well.

C. Steady-State Operation

Typical OH emission images, taken during steady-state operation, are shown in Fig. 14. Time averaged images have been calculated

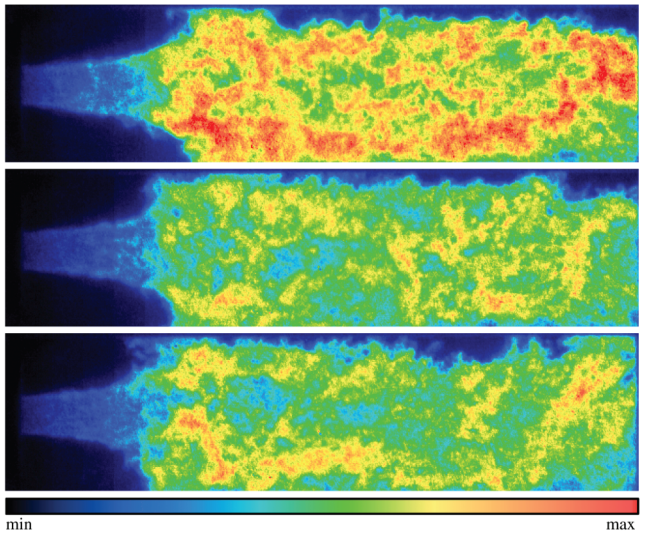

a) Instantaneous OH emission

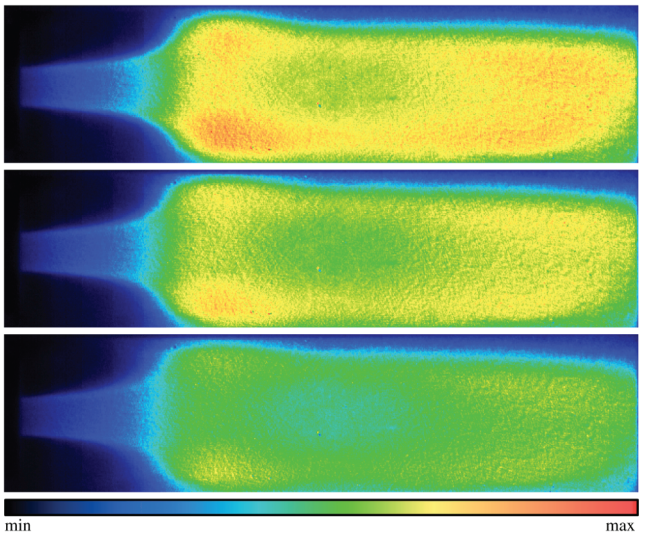

b) Time averaged OH emission

Fig. 14 OH emission images at operating point C during phase 1 (supercritical, top), phase 2 (near critical, middle) and phase 3 (subcritical, bottom).

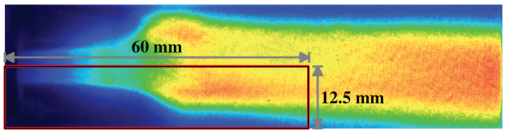

a) Flame region of interest

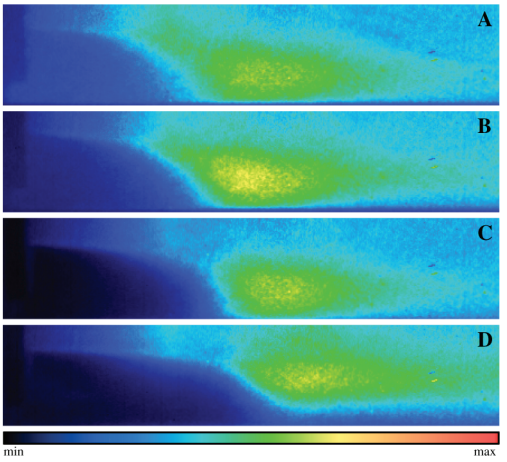

b) Subcritical conditions (phase 3), $P_r<1$, A) $J=3.95$, B) $J=6.94$, C) $J=10.16$, D) $J=25.04$

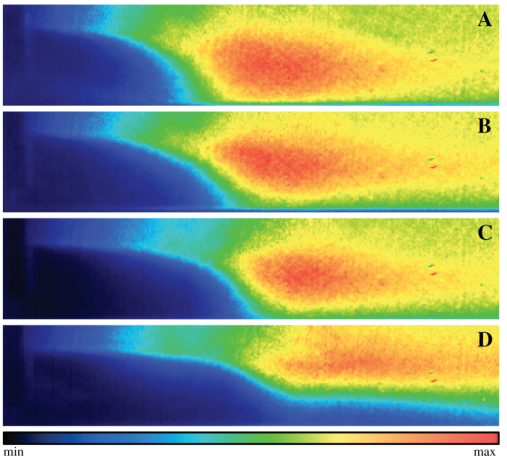

c) Supercritical conditions (phase 1), $P_r<1$, A) $J=2.69$, B) $J=4.70$, C) $J=6.90$, D) $J=16.92$

Fig. 15 Time averaged near-injector CH emission images during sub- and supercritical conditions.

from 8192 single-emission images each, representing a total recording time of 1.024 s. The flame spreading angle increases only slightly with decreasing chamber pressure. In addition, the flame shape in general does not change dramatically from sub- to supercritical conditions. It is widely accepted that the VR and J influence the atomization characteristics in typical coaxial injection. Time averaged CH emission images in Fig. 15 show the influence of the momentum flux ratio on the near-injector flame shape at sub- and supercritical pressures covering the operating points A–D, as defined in Table 2. The region of interest is shown in Fig. 15a. It can be seen from these images that an increasing methane injection velocity (and, thus, an increasing VR and J) leads to a constriction of the flame and a decreasing spreading angle. This was also observed by Juniper et al. [26] in LOX/H_2 flames at elevated pressures. Similar to LOX/H_2 flames, the LOX/CH_4 flame follows the liquid oxygen jet right after injection. At a distance of approximately 5–6d_i, the liquid jet begins to disintegrate and the flame expands. This characteristic flame expansion can be explained by the decreasing shear forces of the coflowing methane on the LOX jet at a certain distance from the injector face. In addition, strong vaporization of the oxygen leads to an expansion and, thus, to a widening of the flame as described for LOX/H_2 flames [27]. With this configuration, the flame expansion starts further upstream at lower J. With the same injection velocity of the LOX jet, a lower J corresponds to a lower methane injection velocity and momentum flux. However, the influence of neighboring injector elements as found in typical liquid propellant rocket engines is neglected. It is possible that an increasing momentum flux ratio will lead to an earlier flame expansion with a multi-injector faceplate. Because the coaxial streams in such a configuration are constricted by neighboring streams, the thinning of the methane flow is less. As a result, shear forces between the gaseous stream and the liquid jet are present further downstream, which results in a better atomization and a stronger flame expansion. It is also visible in Fig. 15 that the first main combustion zone right after expansion of the flame is stretched axially at very high momentum flux ratios (operating point D).

The color scale has been normalized with the maximum emission intensity during phase 1 for each operating point. It is evident from Fig. 15 that the total flame emission intensity decreases with decreasing chamber pressure. With a reduction of the combustion chamber pressure from 60 to 40 bar, the CH emission intensity is decreased by about 35–40% whereas the OH emission intensity drops only by about 20–27%. In general, a reduction of the chamber pressure comes along with an increasing momentum flux ratio, which in turn increases the emission intensity. This effect is stronger at higher momentum flux ratio levels (corresponding to smaller

methane injection diameters d_o). Thus, the total emission intensity drop depends on the injector element.

The application of a deconvolution using the Abel transform to an averaged OH emission image at supercritical conditions is shown in Fig. 16b. The code for calculation of the deconvolution is based on Ostrovskii et al. [28]. To reduce the noise that is produced by the image intensifier, the time averaged OH emission image has been filtered using a 3×3 pixel adaptive Wiener filter. As described by Pham [29], the Wiener filter preserves slightly better sharpness compared with a mean filter. That is important, especially in the region right behind the injection plane where strong emission gradients define the thin reacting shear layer around the LOX jet.

In addition to the Abel transform, the magnitude of the gradient $\nabla \bar{I}_{\mathrm{OH}}$ of the averaged OH emission as shown in Fig. 16a,

$$G(x,y) = \left(\left(\frac{\partial I_{\mathrm{OH}}(x,y)}{\partial x} \boldsymbol{e}_x \right)^2 + \left(\frac{\partial I_{\mathrm{OH}}(x,y)}{\partial y} \boldsymbol{e}_y \right)^2 \right)^{1/2} \tag{10}$$

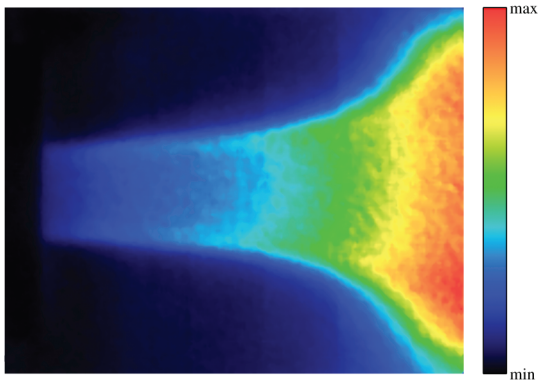

a) Time averaged OH emission

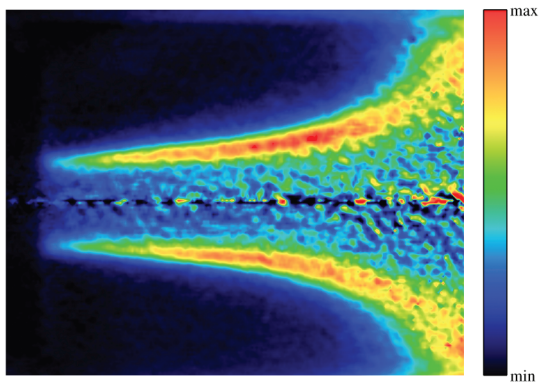

b) Deconvolution of the averaged OH emission

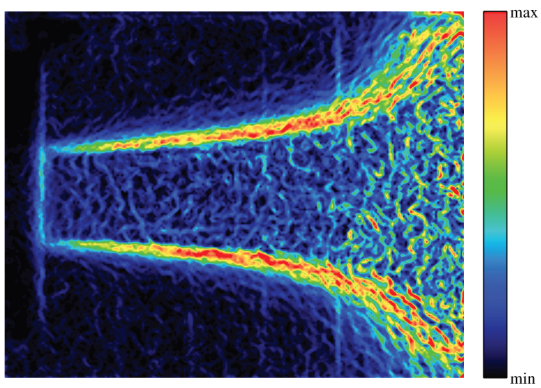

c) Magnitude of the gradient $\nabla \bar{I}_{\mathrm{OH}}$ of the averaged OH emission

Fig. 16 OH emission images during phase 1 (supercritical), (30 × 25 mm) of operating point C: $J = 6.90$, VR = 12.20.

is given in Fig. 16c. Both images illustrate the flame anchoring in the wake of the LOX post and give an impression of the reacting shear layer between the liquid oxygen and the gaseous methane. In particular, the small gradients in emission intensity right behind the lip of the LOX tube are more visible in Fig. 16c. The extended interchangeable methane injector nut is also clearly visible in this figure. On the other hand, the Abel transform can be used to get an idea of the dimension of the reacting shear layer between the liquid oxygen and the methane. It can be seen from Fig. 16b that the shear layer grows continuously with increasing distance from the injection plane.

Even if theoretical investigations show differing characteristics between the binary system CH_4/O_2 and the H_2/O_2 system, no well-defined difference is visible in the emission images at sub- and supercritical conditions. In this context, one needs to note that in a reacting flow there is always additional species like H_2O participating that could influence the atomization of the liquid jet.

Compared with former studies of LOX/hydrogen combustion, the results presented here show similar characteristics. As observed in coaxial injection of liquid oxygen and gaseous hydrogen, the flame anchors near the LOX post tip and follows the oxygen jet [30]. The reacting shear layer near the LOX post tip is slightly thicker than in LOX/hydrogen combustion. Nevertheless, a quantitative comparison should be handled with care based on the different experimental setups, operating conditions, and diagnostic systems.

VII. Conclusions

Flame stabilization in LOX/Methane combustion using a single shear coaxial injector has been investigated during both ignition and steady-state operation. An optically accessible subscale combustion chamber has been used to detect OH and CH emission in the near-injector region. Only small differences have been found between OH and CH emission images during steady-state operation. High-pressure flame emission spectra from a position 70 mm downstream of the injector face have shown significant disparities compared with those from a CH_4/O_2 Bunsen burner at ambient pressures. The high-pressure flame emission spectra are very similar to those from high-pressure LOX/H_2 combustion studies.

A very good reproducible startup characteristic has been detected that shows the ignition of a GO_2/CH_4 mixture at sonic injection velocities. It can be assumed that this ignition characteristic is also possible in LOX/H_2 combustion in similar operating conditions. As soon as oxygen is provided in a liquid or subcooled state, the flame anchors in the wake of the LOX post tip at all operating conditions.

Steady-state operation was performed at sub- to supercritical pressures between 40 and 60 bar. Similar to observations of LOX/H_2 combustion, the near-injector flame surrounds the LOX jet within the first 4–5d_i from the injection plane. At about 5–6d_i, the flame expands due to the disintegration of the LOX jet and the high vaporization rate. The application of a deconvolution to time averaged flame emission images using the Abel transform shows a reacting shear layer between the liquid oxygen and the gaseous methane, which continuously grows with increasing distance from the injector face. The near-injector flame shape is influenced by the injection parameters, such as VR and J. In conformance with LOX/H_2 combustion studies, an increasing momentum flux ratio leads to both a smaller spreading angle and a more constricted flame.

In summary, the LOX/methane flame behaves similarly to the LOX/hydrogen flame. Taking into account the slightly different experimental setups and operating conditions of previous LOX/H_2 investigations, the results presented here are in good conformance with those for LOX/hydrogen flames. Both the near-injector flame anchoring and the flame emission further downstream show similar characteristics. With the operating conditions presented here, the reacting shear layer of the LOX/methane flame seems to be slightly thicker than in comparable LOX/hydrogen flames. However, with respect to the aforementioned differences between the optical setups, the anchoring zone very close to the LOX post tip should be further investigated.

Future investigations should also focus on the influence of injector dimensions, such as the LOX post wall thickness on the near-injector flame shape. In addition, the influence of a recessed LOX tube as used in most liquid propellant rocket engine injectors should be studied.

Acknowledgments

The support of the P8 team with the assistance of D. Suslov is gratefully acknowledged. In addition, the first author would like to thank W. Clauß for contributing the Bunsen burner emission spectra.

References

[1] Burkhardt, H., Sippel, M., Herbertz, A., and Klevanski, J., "Kerosene Vs Methane: A Propellant Tradeoff for Reusable Liquid Booster Stages," *Journal of Spacecraft and Rockets*, Vol. 41, No. 5, 2004, pp. 762–769. doi:10.2514/1.2672

[2] Mayer, W., and Tamura, H., "Propellant Injection in a Liquid Oxygen/Gaseous Hydrogen Rocket Engine," *Journal of Propulsion and Power*, Vol. 12, No. 6, 1996, pp. 1137–1147. doi:10.2514/3.24154

[3] Candel, S., Herding, G., Snyder, R., Scouaire, P., Rolon, C., Vingert, L., Habiballah, M., Grisch, F., Péalat, M., Bouchardy, P., Stepowski, D., Cessou, A., and Colin, P., "Experimental Investigation of Shear Coaxial Cryogenic Jet Flames," *Journal of Propulsion and Power*, Vol. 14, No. 5, 1998, pp. 826–834. doi:10.2514/2.5346

[4] Herding, G., Snyder, R., Rolon, C., and Candel, S., "Investigation of Cryogenic Propellant Flames Using Computerized Tomography of Emission Images," *Journal of Propulsion and Power*, Vol. 14, No. 2, 1998, pp. 146–151. doi:10.2514/2.5279

[5] Ferraro, M., Kujala, R. J., Thomas, J.-L., Glogowski, M. J., and Micci, M. M., "Effects of GH_2/LOX Velocity and Momentum Ratios on Shear Coaxial Injector Atomization," *Journal of Propulsion and Power*, Vol. 18, No. 1, 2002, pp. 209–211. doi:10.2514/2.5920

[6] Singla, G., Scouaire, P., Rolon, C., and Candel, S., "Transcritical Oxygen/Transcritical or Supercritical Methane Combustion," *Proceedings of the Combustion Institute*, Vol. 30, No. 2, Jan. 2005, pp. 2921–2928. doi:10.1016/j.proci.2004.08.063

[7] Singla, G., Scouaire, P., Rolon, J. C., Candel, S., and Vingert, L., "OH Planar Laser-Induced Fluorescence and Emission Imaging in High-Pressure LOx/Methane Flames," *Journal of Propulsion and Power*, Vol. 23, No. 3, 2007, pp. 593–602. doi:10.2514/1.24895

[8] Salgues, D., Mouis, A.-G., Lee, S.-Y., Kalitan, D., Pal, S., and Santoro, R., "Shear and Swirl Coaxial Injector Studies of LOX/GCH4 Rocket Combustion Using Non-Intrusive Laser Diagnostics," AIAA Paper 2006-757, 2006.

[9] Zong, N., and Yang, V., "Near-Field Flow and Flame Dynamics of LOX/Methane Shear-Coaxial Injector Under Supercritical Conditions," *Proceedings of the Combustion Institute*, Vol. 31, No. 2, Jan. 2007, pp. 2309–2317. doi:10.1016/j.proci.2006.08.106

[10] Zong, N., Ribert, G., and Yang, V., "A Flamelet Approach for Modeling of Liquid Oxygen (LOX)/Methane Flames at Supercritical Pressures," AIAA Paper 2008-946, 2008.

[11] Mayer, W. O. H., and Smith, J. J., "Fundamentals of Supercritical Mixing and Combustion of Cryogenic Propellants," *Liquid Rocket Thrust Chambers: Aspects of Modelling, Analysis, and Design*, edited by V. Yang, M. Habiballah, J. Hulka, and M. Popp, Vol. 200, AIAA Progress in Aeronautics and Astronautics, AIAA, Reston, VA, 2004.

[12] Smith, J. J., "High Pressure LOx/H2 Rocket Engine Combustion," Dissertation, University of Adelaide, 2007.

[13] Lux, J., Suslov, D., Bechle, M., Oschwald, M., and Haidn, O., "Investigation Of Sub- And Supercritical LOX/Methane Injection Using Optical Diagnostics," AIAA Paper 2006-5077, 2006.

[14] Schmidt, R., and Wagner, W., "A New Form of the Equation of State for Pure Substances and Its Application to Oxygen," *Fluid Phase Equilibria*, Vol. 19, No. 3, 1985, pp. 175–200. doi:10.1016/0378-3812(85)87016-3

[15] Setzmann, U., and Wagner, W., "A New Equation of State and Tables of Thermodynamic Properties for Methane Covering the Range from the Melting Line to 625 K at Pressures Up to 1000 MPa," *Journal of Physical and Chemical Reference Data*, Vol. 20, No. 6, 1991, pp. 1061–1151.

[16] Younglove, B. A., "Thermophysical Properties of Fluids. I. Argon, Ethylene, Parahydrogen, Nitrogen, Nitrogen Triuoride, and Oxygen," *Journal of Physical and Chemical Reference Data*, Vol. 11, No. 1, Feb. 1982, pp. 1–354.

[17] Delplanque, J.-P., "Liquid-Oxygen Droplet Vaporization and Combustion: Analysis of transcritical behaviour and application to liquid-rocket combustion instability," Dissertation, University of California Irvine, 1992.

[18] Mayer, W., Ivancic, B., Schik, A., and Hornung, U., "Propellant Atomization in LOX/GH2 Rocket Combustors," AIAA Paper 1998-3685, 1998.

[19] Delplanque, J.-P., and Sirignano, W. A., "Numerical Study of the Transient Vaporization of an Oxygen Droplet at Sub- and Super-Critical Conditions," *International Journal of Heat and Mass Transfer*, Vol. 36, No. 2, 1993, pp. 303–314. doi:10.1016/0017-9310(93)80006-G

[20] Lux, J., Zell, D., Suslov, D., and Haidn, O., "Untersuchungen transkritischer CH4/O2-Mischungen," Deutscher Luft- und Raumfahrtkongress, Braunschweig, Germany, 2006.

[21] Nicoli, C., Haldenwang, P., and Daou, J., "Substitute Mixtures for LOX Droplet Vaporization Study," *Combustion Science and Technology*, Vol. 112, No. 1, 1996, pp. 55–74. doi:10.1080/00102209608951949

[22] Singla, G., Scouaire, P., Rolon, J. C., and Candel, S., "Flame Stabilization in High Pressure LO_X/GH_2 and GCH_4 Combustion," *Proceedings of the Combustion Institute*, Vol. 31, No. 2, Jan. 2007, pp. 2215–2222. doi:10.1016/j.proci.2006.07.094

[23] Richecoeur, F., Scouaire, P., Ducruix, S., and Candel, S., "High-Frequency Transverse Acoustic Coupling in a Multiple-Injector Cryogenic Combustor," *Journal of Propulsion and Power*, Vol. 22, No. 4, 2006, pp. 790–799. doi:10.2514/1.18539

[24] Mayer, W., Schik, A., and Schaeer, M., "Injection and Mixing Processes in High-Pressure Liquid Oxygen/Gaseous Hydrogen Rocket Combustors," *Journal of Propulsion and Power*, Vol. 16, No. 5, 2000, pp. 823–828. doi:10.2514/2.5647

[25] Lux, J., Suslov, D., and Haidn, O., "On Porous Liquid Propellant Rocket Engine Injectors," *Aerospace Science and Technology*, Vol. 12, No. 6, Sept. 2008, pp. 469–477.doi: 10.1016/j.ast.2007.11.004.

[26] Juniper, M., Tripathi, A., Scouaire, P., Rolon, J.-C., and Candel, S., "Structure of Cryogenic Flames at Elevated Pressures," *Symposium (International) on Combustion*, Vol. 28, No. 1, 2000, pp. 1103–1109. doi:10.1016/S0082-0784(00)80320-3

[27] Herding, G., Snyder, R., Scouaire, P., Rolon, C., and Candel, S., "Flame Stabilization in Cryogenic Propellant Combustion," *26th International Symposium on Combustion*, The Combustion Institute, Pittsburgh, PA, Aug. 1996, pp. 2041–2047.

[28] Ostrovskii, Y. I., Butusov, M. M., and Ostrovskaya, G. V., *Holographic Interferometry*, Izdatelstvo Nauka, Moscow, 1977.

[29] Pham, T. D., "An Image Restoration by Fusion," *Pattern Recognition*, Vol. 34, No. 12, 2001, pp. 2403–2411. doi:10.1016/S0031-3203(00)00164-3

[30] Candel, S., Juniper, M., Singla, G., Scouaire, P., and Rolon, C., "Structure and Dynamics of Cryogenic Flames at Supercritical Pressures," *Combustion Science and Technology*, Vol. 178, No. 1–3, Jan. 2006, pp. 161–192. doi:10.1080/00102200500292530

[31] Lemmon, E. W., Huber, M. L., and McLinden, M. O., *NIST Reference Fluid Thermodynamic and Transport Properties Database (REFPROP): Version 8.0*, National Institute of Standards and Technology, Boulder, CO, 2007.

D. Talley
Associate Editor